Absence of spin transport in amorphous YIG evidenced by nonlocal spin transport experiments

Liupeng Yang,[1] Yaoyu Gu,[1] Lina Chen,[1,2,*] Kaiyuan Zhou,[1] Qingwei Fu,[1] Wenqiang Wang,[1] Liyuan Li,[1] Chunjie Yan,[1]
Haotian Li,[1] Like Liang,[1] Zishuang Li,[1] Yong Pu,[2,†] Youwei Du,[1] and Ronghua Liu ●[1,‡]

[1]*National Laboratory of Solid State Microstructures, School of Physics and Collaborative Innovation Center of Advanced Microstructures,*
Nanjing University, Nanjing 210093, China
[2]*New Energy Technology Engineering Laboratory of Jiangsu Province and School of Science,*
Nanjing University of Posts and Telecommunications, Nanjing 210023, China

It remains highly controversial whether long-distance spin transport or only Joule heating without spin transport exists in the disordered magnetic amorphous $Y_3Fe_5O_{12}$ (a-YIG). Here, we carefully check and analyze the origin of the observed electrical signals in the Py/a-YIG/Pt-based nonlocal spin-transport experiments with both horizontal and vertical geometries, based on the ferromagnetic resonance (FMR)-induced spin pumping and inverse spin Hall effect. In all lateral nonlocal devices with a distance from 2.0 μm to 200 nm and vertical structures with a $\geqslant$40-nm-thick a-YIG spacer layer, the spin-current-induced direct voltage peak signal is absent under FMR conditions, indicating that a-YIG does not possess long-distance spin transport. Furthermore, we demonstrate that a weak spin-torque FMR voltage signal, which gradually reduces to zero with increasing a-YIG thickness in the vertical geometry, is attributed to the leaked spin rectification voltage generated in the Py layer due to the electric leakage between the top Pt layer and the bottom Py layer through the pinhole defects in the thin middle a-YIG layer. Additionally, we find an improvement of the interfacial spin-mixing conductance due to spin accumulation in the interface of a-YIG/Py, which can significantly enhance spin-orbit torque efficiency in the ferromagnet/heavy metal systems with a disordered magnetic a-YIG buffer layer.

I. INTRODUCTION

Yttrium iron garnets (YIGs) have been intensively studied due to their unique properties, such as ultralow magnetic damping and insulating nature [1–3]. The ultralow magnetic damping can achieve a high-efficiency ferromagnetic (FM) resonance (FMR)-driven spin-pumping effect because the FMR cone angle is inversely proportional to the damping constant [4]. Compared with FM metals, YIGs are electrically insulating ferrimagnetic materials. Therefore, in the most studied nonmagnetic (NM) heavy metal/YIG bilayers, the detected electrical signals come exclusively from spin-related transport phenomena in the NM layer, making it more straightforward to extract spin-related parameters from various electrical detections with high sensitivity and easy accessibility [5]. Additionally, comparing with the conducting electrons in metals and semiconductors, YIGs can deliver spin current more efficiently via spin waves and avoid serious Joule heating issues facing the complementary metal-oxide semiconductor (CMOS) [6]. Therefore, YIG-based magnon devices using spin waves to process information have attracted much attention as promising candidates with low energy consumption and high throughput computation.

A nonlocal spin Seebeck experiment recently demonstrated that thermally excited magnons could travel $\geqslant$120 μm with

as high as 73 μm spin diffusion length in YIG film at $T = 23$ K [7]. Then long-distance transport of coherent magnons in YIG film was also proved using the electrical excitation and detection based on the spin Hall effect (SHE) and its inverse process (ISHE) in the adjacent Pt layer [8]. The magnon spin-diffusion length λ is as long as 9.4 μm in 200-nm-thick YIG at room temperature. Long-distance transport of all these magnons carrying spin current is realized in crystalline or epitaxial ferrimagnetic YIGs. However, the crystalline YIG also exhibits some disadvantages for its application in magnonic devices, such as a magnon spectrum gap and the highly anisotropic nature of magnon transport [9,10]. Very recently, Wesenberg *et al.* [9] claimed that long-distance spin transport ($\lambda \sim 100$ μm) was also observed in the disordered magnetic amorphous YIG film based on their nonlocal spin Seebeck experiments and further argued that highly efficient spin transport in this disordered magnetic system was related to the strong local exchange interaction. Subsequently, Gomez-Perez *et al.* [11] argued that the temperature-dependent voltage signal measured by the nonlocal spin Seebeck method was attributed to the drop of the a-YIG resistivity caused by Joule heating rather than spin transport.

To solve the controversy of long-distance spin transport in amorphous YIG, here, we carefully perform nonlocal FMR-induced spin-pumping ISHE experiments using both horizontal and vertical geometries to investigate spin transport in amorphous YIG. In all horizontal nonlocal devices with a distance from 2.0 μm to 200 nm and vertical structures with a $\geqslant$40-nm-thick a-YIG spacer layer, we do not observe

*chenlina@njupt.edu.cn
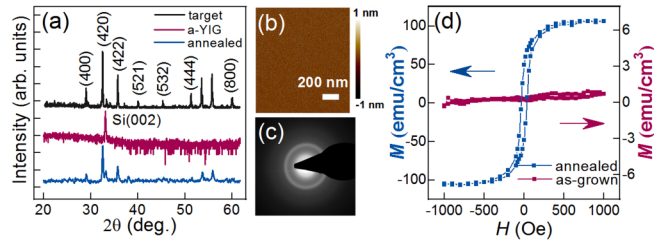†puyong@njupt.edu.cn
‡rhliu@nju.edu.cn

FIG. 1. (a) X-ray diffraction (XRD) patterns of the YIG target, 40-nm-thick as-grown and annealed YIG film. (b) Atomic force microscopy (AFM) image of 20-nm-thick as-grown YIG film. (c) The selected area electron diffraction (SAED) pattern of as-grown YIG film obtained using transmission electron microscopy (TEM), suggesting amorphous phase. (d) M-H curves of the 40 nm as-grown and annealed YIG films obtained at room temperature.
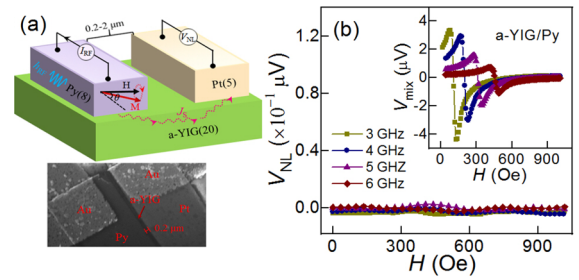

FIG. 2. (a) The schematic of the lateral nonlocal spin-pumping inverse spin Hall effect (ISHE) experiment setup and scanning electron microscopy (SEM) image of the device. A radiofrequency current (I_{RF}) is applied in the Py(8) strip, and the in-plane external magnetic field H forms an angle of $\theta = 30°$ with the direction of I_{RF}. A lock-in amplifier is connected to the Pt(5) strip to detect the spin-current-induced direct current (dc) voltage due to its ISHE. (b) The representative field-dependent nonlocal voltage V_{NL} spectra detected by the Pt strip, performed at four different exciting frequencies $f = 3, 4, 5,$ and 6 GHz, does not show any distinguishable peak under Py ferromagnetic resonance (FMR) conditions. The inset shows the clear antisymmetric spin-torque (ST) FMR voltage signal detected by the Py strip.

any nonlocal spin-pumping-ISHE-induced direct current (dc) voltage peak signal under the Py FMR condition, indicating that long-distance spin transport is absent in disordered magnetic a-YIG. However, we demonstrate a considerable spin accumulation in the interface of a-YIG/Py due to the improvement of the interfacial spin-mixing conductance by comparing the spin-torque (ST)-FMR results of a-YIG/Py/Pt with that of Py/Pt samples.

II. RESULTS AND DISCUSSION

A. Experimental detail and the characteristics of a-YIG film

The Pt, permalloy (Py), and amorphous YIG layers were deposited at room temperature under 3.7 mTorr Ar using dc and radiofrequency (RF) magnetron sputtering, respectively, with $<3 \times 10^{-8}$ Torr base pressure, as previous reported [12,13]. No postannealing was performed for the as-grown multilayer-based devices to avoid as-grown amorphous YIG recrystallization. X-ray diffraction (XRD), atomic force microscopy (AFM), and transmission electron microscopy (TEM) were used to characterize the crystal structure and surface morphology of a-YIG films. The magnetic properties of films were characterized by the vibrating sample magnetometer (VSM). To fabricate the devices used in nonlocal spin-pumping ISHE and ST-FMR measurements, we patterned the films into 4×17 and $5 \times 17 \mu m^2$ rectangular shapes by combining photolithography, electron beam lithography, and ion milling.

We first characterized the crystal structures of the YIG target and the as-grown and annealed YIG films by using XRD. Our YIG sputtering target shows a pure polycrystalline YIG phase [12,14], as shown in Fig. 1(a). The XRD spectrum of 40-nm-thick as-grown YIG film on Si substrate only shows the (002) peak of the substrate Si at $2\theta \approx 33°$. After 40 nm as-grown YIG film was annealed at 900 °C for 1 h [12], the diffraction peaks corresponding to YIG appeared, suggesting the as-grown amorphous YIG film was recrystallized and became polycrystalline phase after high-temperature annealing, consistent with our previous study [12]. The AFM image of the 20-nm-thick as-grown YIG shows that its surface roughness is only ∼0.5 nm [15], suggesting the high quality of the film [Fig. 1(b)]. In addition, we further characterized the as-grown YIG structure and its magnetic properties by

TEM and VSM, respectively. The TEM was performed using the Tecnai F20 electron microscope (FEI Co, USA), and the related selected area electron diffraction (SAED) pattern is shown in Fig. 1(c). A clear halo pattern of the as-grown YIG is observed, which is the typical diffraction pattern for amorphous materials [16]. Furthermore, the measured M-H curve of the as-grown YIG film at room temperature shows a paramagnetic behavior without hysteresis, shown in Fig. 1(d), consistent with the amorphous YIG film reported in the previous work [11]. Therefore, the obtained as-grown YIG film is an amorphous structure, also named as a-YIG below.

B. Lateral nonlocal spin-pumping ISHE results

Spin transport in 20-nm-thick as-grown a-YIG films was first investigated by the nonlocal spin-pumping ISHE method with the horizontal geometry at room temperature, as shown in Fig. 2(a) [8,17]. The test devices were constructed of Py and Pt strips with a rectangular shape of $4 \times 17 \mu m^2$ pattern on a 20-nm-thick a-YIG film. The Py and Pt strips were separated with a distance ranging from 2 μm to 200 nm. The thicknesses of the Py and Pt strips were 8 and 5 nm, respectively. The Py strip is the injector of spin currents due to the spin-pumping effect under FMR conditions, and the Pt strip acts as the spin detector because it has an ISHE. A RF current I_{RF} was applied into the Py strip, which can effectively excite FMR when its magnetization is perpendicular to the RF current-induced Oersted field h_{RF} direction (parallel to the I_{RF} direction). However, the spin-pumping ISHE signal is maximum as Py magnetization is oriented perpendicular to the I_{RF} direction. Therefore, we performed nonlocal spin-pumping ISHE and ST-FMR measurements described below at a representative angle $\theta = 30°$ between the applied magnetic field and the RF current direction by trading off a reduction in the oscillating angle FMR for the sizable dc voltage signal generated from the spin-pumping ISHE. If the FMR of the

Py layer is excited by I_{RF}, the precession of the magnetization will inject a pure spin current into the adjacent a-YIG layer from the Py layer [18,19]. A phase-sensitive lock-in amplifier detects the nonlocal dc voltage signal via ISHE if the considerable pumping spin currents can transport through the a-YIG layer into a 5-nm-thick Pt layer [20,21]. However, Fig. 2(b) shows that no voltage peak signal is observed for the horizontal geometry devices with the gap from 2.0 μm to 200 nm when the magnetic field scans from 0 to 1000 Oe at several exciting frequencies $f = 3$–6 GHz, indicating that the previously reported long-distance spin transport in the disordered magnetic a-YIG film is not observed in our lateral nonlocal devices. To exclude the possibility that the lack of spin-current injection causes no observed dc voltage signal at the a-YIG/Py interface due to possible improper spin-pumping experiments, we also directly detected the local ST-FMR signal of the Py strip of the same lateral nonlocal device. The observed antisymmetric ST-FMR voltage signal in a-YIG/Py strip demonstrates that the FMR of the Py layer can be effectively excited in our test devices, shown in the inset of Fig. 2(b), indicating there are spin currents injected into a-YIG by the spin-pumping effect.

C. Vertical nonlocal spin-pumping ISHE results

To further detect possible short-distance spin transport in a-YIG film, we adopted the vertical stack structure Py(8)/a-YIG(t)/Pt(5) (5 nm $\leqslant t \leqslant$ 40 nm) for nonlocal spin transport test devices [22,23]. Figure 3(a) shows the vertical nonlocal spin-pumping ISHE experiment setup, where only the top Pt layer is electrically connected with a signal generator and a lock-in amplifier. The RF current I_{RF} passing through the Pt layer generates an oscillating spin current J_S via SHE and an alternating Oersted field H_{Oe}, which can drive the magnetization oscillation of the Py layer around the applied static magnetic field H. Then the magnetization precession of the Py layer causes an oscillating resistance due to its anisotropic magnetoresistance (AMR) effect [13,24]. As a result, the oscillating resistance and the induced alternating current I_{RF} in the Py layer produces a dc voltage V_{mix} across the Py strip. This procedure is also called the *rectification effect* [24,25]. Additionally, the magnetization precession of the Py layer also pumps a spin current into the adjacent a-YIG layer due to the so-called spin-pumping effect [26–28]. The in-plane external magnetic field H is applied to form an angle of 30° with the RF current I_{RF} direction, like the horizontal nonlocal structure above, simultaneously ensuring that the FMR of the Py layer can be effectively excited and the spin-pumping signal is detectable via ISHE of Pt.

In principle, the symmetrical dc voltage signal V_{mix} is detectable on both sides of the Pt strip in this vertical nonlocal device if the a-YIG layer is an ideal insulator without pinhole defects and has long-distance spin transport. The reason is that antisymmetrical dc voltage raised from the AMR-induced rectification in the Py layer is isolated electrically from the top Pt layer by the electrical insulator a-YIG layer. Note that the rectification voltage contributed from spin Hall magnetoresistance and anomalous Hall effect is expected to be negligible in the Py/a-YIG/Pt devices due to the paramagnetic property of a-YIG [29,30].
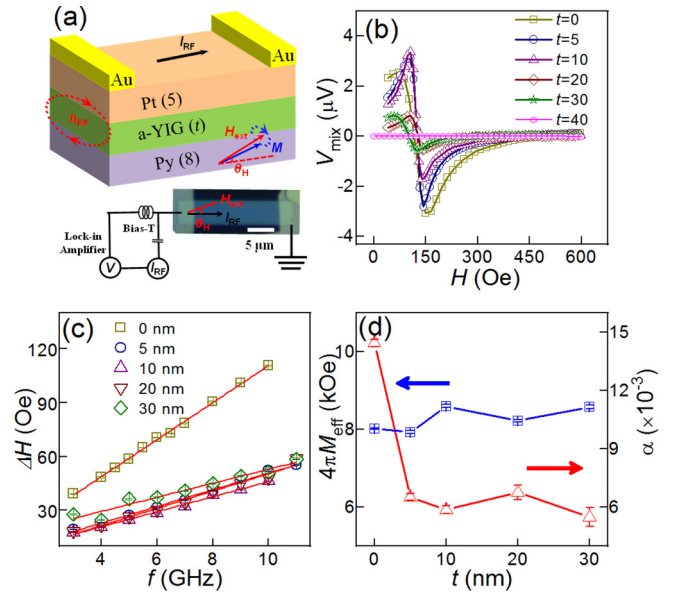

FIG. 3. (a) Schematic of the nonlocal spin-transport experimental setup in the vertical stack structure Py(8)/a-YIG(t)/Pt(5), analogous to ST-FMR of bilayer Py/Pt, where a radiofrequency current I_{RF} is along the longitudinal direction of sample, with an in-plane external magnetic field H forming $\theta = 30°$ angle. (b) Field-dependent direct current (dc) voltage V_{mix} spectra obtained at $f = 4$ GHz for the Py(8)/a-YIG(t)/Pt(5) samples with labeled thickness t. (c) Symbols: ΔH vs f experimental data for the samples. The solid lines are the linear fitting curves. (d) Dependence of the effective demagnetization field $4\pi M_{eff}$ and the magnetic damping α on the thickness t of the space layer a-YIG.

We measured the field-dependent dc voltage signal V_{mix} of the Py(8)/a-YIG(t)/Pt(5) device by varying the excitation frequency f from 3 to 11 GHz. Figure 3(b) shows the representative V_{mix} spectra of the vertical nonlocal devices with different thicknesses of a-YIG at $f = 4$ GHz. The field-dependent V_{mix} curve of the vertical structure Py(8)/Pt(5) without the spacer layer a-YIG shows a typical ST-FMR spectrum, which can be well fitted by the Lorentzian function as follows:

$$V_{mix} = V_S \frac{\Delta H^2}{(\mu_0 H - \mu_0 H_r)^2 + \Delta H^2} + V_A \frac{\Delta H(\mu_0 H - \mu_0 H_r)}{(\mu_0 H - \mu_0 H_r)^2 + \Delta H^2},$$
(1)

where the parameters of V_S, V_A, ΔH, and $\mu_0 H_r$ are the magnitude of the symmetric component, the antisymmetric component, the linewidth, and the FMR field, respectively [31,32]. These parameters can be extracted by fitting the experimental data using Eq. (1). For the samples with the insulating a-YIG spacer layer, we observe a gradual reduction in the amplitude of the total signal V_{mix} and the symmetric component V_S with increasing the thickness of a-YIG, especially for $t \leqslant 20$ nm. When $t \geqslant 40$ nm, no detectable voltage peak signal V_{mix} can be observed within the noise background level of $\leqslant 0.01$ μV. The observed V_{mix} signals for the samples with $t \leqslant 30$ nm a-YIG are more likely to come from the spin rectification voltage in the bottom layer Py due to the electric leakage between the top layer Pt and Py through the pinhole defects in the thin middle insulating a-YIG layer [33]. Many

previous reports have proven that a single Py layer can generate a considerable ST-FMR voltage signal due to the spin-rectification effect [34,35]. As expected, the pinhole defects will decrease with increasing the thickness of the deposited a-YIG layer and are covered completely when the insulating a-YIG layer is $\geqslant 40$ nm in this paper. Additionally, the resistance of Py/a-YIG/Pt devices between the top Au electrodes significantly increases from ~ 132 to $\sim 178\ \Omega$ with increasing the a-YIG spacer layer thickness t from 0 to 40 nm. While $t \geqslant 40$ nm, the resistance of the devices keeps almost constant ($\sim 178\ \Omega$) and is close to that of the 5 nm single Pt layer, confirming that the thick a-YIG ($t \geqslant 40$) inserting layer without pinhole defects causes electrical isolation between Py and Pt layers. Therefore, the absent voltage peak signal in the 40-nm-thick a-YIG sample indicates that the rectification voltage generated in the Py layer and the spin currents due to spin pumping in the bottom layer Py are both blocked entirely by the spin and electrical insulating disordered magnetic a-YIG.

The effective spin-mixing conductance $g_{\mathrm{eff}}^{\uparrow\downarrow}$ can also be used to characterize the efficiency of spin transport or spin pumping in the NM/FM systems [27,36]. Here, $g_{\mathrm{eff}}^{\uparrow\downarrow}$ is related to the enhancement in the effective magnetic damping α as follows [26,37]:

$$g_{\mathrm{eff}}^{\uparrow\downarrow} = \frac{4\pi M_S d_{\mathrm{Py}}}{g\mu_B}(\alpha_{\mathrm{HM/Py}} - \alpha_{\mathrm{Py}}), \qquad (2)$$

where M_S is the saturation magnetization of the Py layer, d_{Py} is the thickness of the Py layer, g is the electron g factor, and μ_B is the Bohr magneton. Figure 3(c) shows the dependence of excitation frequency f on the extracted linewidth ΔH for Py(8)/a-YIG(t)/Pt(5) with different thicknesses t. The frequency-dependent linewidth allows us to obtain the magnetic damping α by a linear fitting using $\Delta H = (2\pi/\gamma)\alpha f + \Delta H_0$, where ΔH_0 is the inhomogeneous line broadening. In addition, the effective demagnetization field $4\pi M_{\mathrm{eff}}$ is also determined from the Kittel formula: $f = (\gamma\mu_0/2\pi)[H_r(H_r + 4\pi M_{\mathrm{eff}})]^{1/2}$, where $\gamma/2\pi$ is the gyromagnetic ratio. All samples with or without the inserting a-YIG spacer layer show a near-constant $4\pi M_{\mathrm{eff}} \sim 8.1$ kOe within the experimental accuracy [Fig. 3(d)], confirming that the as-grown a-YIG film exhibits the paramagnetic behavior [11]. However, the magnetic damping α dramatically decreases to a value of 6.5×10^{-3}, close to that of a single 8-nm-thick Py film, from 14.5×10^{-3} in the bilayer Py(8)/Pt(5) when just inserting the 5-nm-thick a-YIG spacer between Py and Pt layers [Figs. 3(c) and 3(d)]. Based on the above Eq. (2), the effective spin-mixing conductance $g_{\mathrm{eff}}^{\uparrow\downarrow}$ drops dramatically to near zero from 2.25×10^{19} m^{-2} by only inserting the 5-nm-thick a-YIG spacer, which indicates that the spin-pumping efficiency is suppressed by the presence of a thin a-YIG spacer, like the inserting layer MgO [38], and further confirms the above argument, absent long-distance spin transport in the as-grown a-YIG layer, obtained by the nonlocal spin-pumping ISHE measurements. Additionally, our results are consistent with the nonlocal spin Seebeck transport study performed by Gomez-Perez *et al.* [11]. The early reported temperature-dependent long-distance transport nonlocal voltage signal could correspond to the dramatic drop of a-YIG
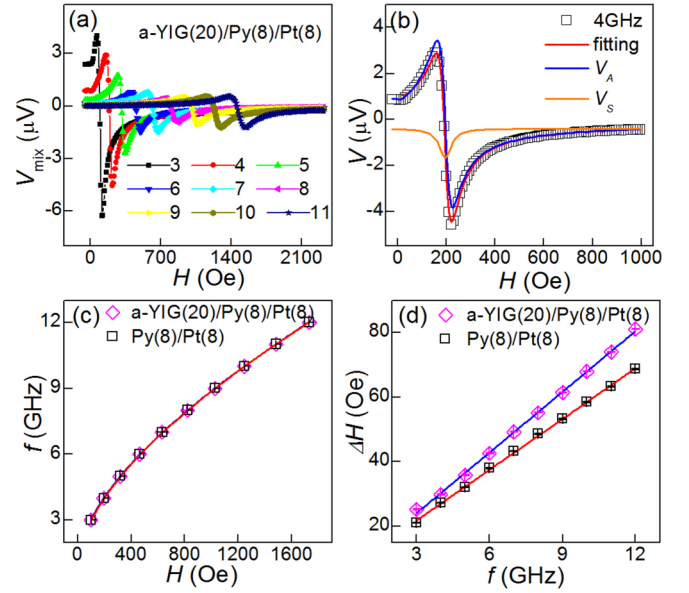

FIG. 4. (a) The magnetic field dependence of V_{mix} for a-YIG(20)/Py(8)/Pt(8) measured at the excitation frequency from 3 to 11 GHz. (b) The representative experimental data and fitting curves of field-dependent V_{mix} at the frequency $f = 4$ GHz. $F_S(H)$ and $F_A(H)$ correspond to the symmetric and antisymmetric Lorentzian functions of V_{mix}, respectively. Dependences of excitation frequency f on (c) resonant field H_r and (d) linewidth ΔH. The solid curves are the fitting results.

resistivity induced by the local Joule heating effect rather than the intrinsic spin or magnon transport [9]. Subsequent theoretical studies also find that the spin-transmission probability and spin conductance both decay exponentially with the localization length in this disordered magnetic system due to the Anderson localization, suggesting that long-distance spin transport is hard to be realized in disordered magnets [39].

D. Spin accumulation in the interface of a-YIG/Py

To further investigate the interfacial spin characteristics of a-YIG/Py, the controlled experiments between a-YIG(20)/Py(8)/Pt(8) and Py(8)/Pt(8) samples were performed at room temperature via the ST-FMR technique. Figure 4(a) shows the magnetic-field-dependent ST-FMR V_{mix} spectra of a-YIG(20)/Py(8)/Pt(8) with different exciting frequency $f = 3$–11 GHz. The representative V_{mix} obtained at $f = 4$ GHz and its Lorentzian function fitting curves are represented in Fig. 4(b). We can extract the symmetric component V_S and antisymmetric component V_A from the obtained V_{mix} spectra by fitting the experimental data with Eq. (1). Based on the symmetry analysis of spin-orbit torques (SOTs), V_S is proportional to the dampinglike torque τ_{DL}, while V_A is attributed to both fieldlike and current-induced Oersted field torques $\tau_{\mathrm{FL+Oe}}$. Like the studied Py/a-YIG(t)/Pt samples above, one can easily see that a-YIG(20)/Py(8)/Pt(8) and Py(8)/Pt(8) samples have the same value of $4\pi M_{\mathrm{eff}}$ (~ 8.7 kOe) because their f vs H_r dispersion curves merge into a single curve, as shown in Fig. 4(c). However, the field-dependent linewidth ΔH results [Fig. 4(d)] show that the a-YIG/Py/Pt has a larger magnetic damping $\alpha \sim 0.0176$
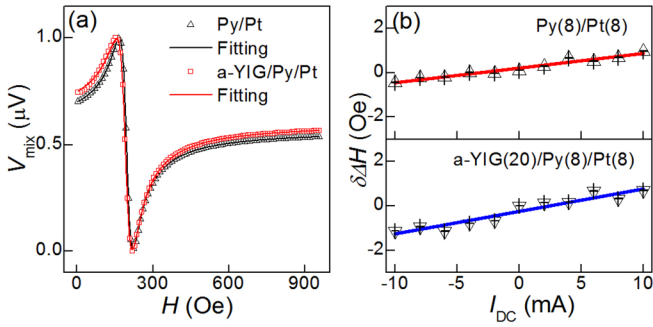
FIG. 5. (a) Normalized experimental data and fitting curves of ST-FMR V_{mix} spectra for Py/Pt and a-YIG/Py/Pt samples at frequency $f = 4$ GHz. The lines are the Lorentzian function fitting curves. (b) Dependence of the linewidth $\delta\Delta H [\delta\Delta H = \Delta H - \Delta H(0)]$ on the direct current (dc) I_{DC} for Py/Pt and a-YIG/Py/Pt samples at $f = 4$ GHz and $\theta_H = 30°$.

than 0.0146 in the Py/Pt sample with a 20.5% increase, which could be caused by the enhancement of the spin-mixing conductance $g_{eff}^{\uparrow\downarrow}$ due to spin accumulation in the a-YIG/Py interface [12,36,40]. However, previous studies indicated that the interface-dependent extrinsic damping of the FM layer, e.g., two-magnon scattering-related damping and spin memory loss existent in the interface of the FM layer [37,41,42], could cause deviation in the determination of $g_{eff}^{\uparrow\downarrow}$.

To further confirm the observed spin accumulation in the interface of a-YIG/Py, we carefully performed and analyzed current-induced SOTs for Py/Pt and a-YIG/Py/Pt samples. Based on the extracted antisymmetric component V_A and symmetric component V_S of ST-FMR V_{mix} spectra, we can quantitatively estimate current-induced dampinglike torque by using the self-calibration technique [22]. Many previous reports have proved that V_A is dominated by Oersted field H_{Oe} in the studied Py/Pt system [22,31]. Thus, the effective SOT efficiency ϑ_{SH} can be estimated by the lineshape analysis as follows:

$$\theta_{SH} = \frac{V_S}{V_A} \frac{e\mu_0 M_S t_N d_F}{\hbar} [1 + (4\pi M_{eff}/H_r)]^{1/2}, \quad (3)$$

where t_N and d_F are the thickness of the Pt and Py layers, M_S the saturation magnetization of samples, μ_0 the vacuum permeability, and $\bar{h}$ reduced Planck's constant. The M_S of the Py/Pt and a-YIG/Py/Pt samples almost have the same value ($\sim$670 emu/cm³), measured individually by VSM. Figure 5(a) shows the representative normalized experimental data and fitting curves of V_{mix} spectra at $f = 4$ GHz for the Py/Pt and a-YIG/Py/Pt samples. The Py/Pt has a SOT efficiency ϑ_{SH} of 0.065, calculated from the lineshape analysis using Eq. (3), very close to the previous reports [22]. The a-YIG/Py/Pt has a more efficient SOT value of 0.084, consistent with the damping enhancement above.

Considering the fieldlike torque and spin-pumping effect induced the deviation of the estimated SOT efficiency, we also can calculate ϑ_{SH} accurately from the dc modulated linewidth of ST-FMR V_{mix} spectra [31,43,44]. Figure 5(b) shows the dc-dependent linewidth $\delta\Delta H [\delta\Delta H = \Delta H - \Delta H(0)]$ for Py/Pt and a-YIG/Py/Pt samples at $f = 4$ GHz. One can easily see that the slope of $\delta\Delta H/\delta I_{DC}$ of the a-YIG/Py/Pt is larger

than that of the Py/Pt sample, suggesting that the former has a larger SOT efficiency, consistent with the analysis of the lineshape above. Based on the linewidth analysis, the SOT efficiency ϑ_{SH} can be expressed by the following formula:

$$\theta_{SH} = \frac{\delta\Delta H/\delta I_{DC}}{\frac{2\pi f}{\gamma} \frac{\sin\theta}{(H_{ext} + 2\pi M_{eff})\mu_0 M_S d_F}} \frac{\hbar}{2e} \frac{R_{Py} + R_{Pt}}{R_{Py}} A_C, \quad (4)$$

where R_{Py} and R_{Pt} are the resistances of the Py and Pt layers, respectively, and A_C is the cross-sectional area of the Pt layer [13,43,45]. The resistances of Py and Pt films were separately measured by the standard four-probe method. Therefore, the calculated SOT efficiencies are 0.06 ± 0.01 and 0.09 ± 0.02 for the Py/Pt and a-YIG/Py/Pt samples from the dc-dependent linewidth data using Eq. (4), approximately consistent with the values estimated by the lineshape analysis above. The results indicate that the a-YIG/Py/Pt sample significantly enhances the SOT efficiency compared with the Py/Pt, consistent with the interfacial spin-mixing conductance discussed above. One may consider that the oxidization of the Py layer exists at the a-YIG/Py interface, causing the enhancement of SOT efficiency for the a-YIG/Py/Pt sample [46,47]. However, the oxidization should be very weak because the extracted effective demagnetization field $4\pi M_{eff}$ from ST-FMR and the saturation magnetization M_S measured by VSM between a-YIG/Py/Pt and Si/SiO₂ (substrate)/Py/Pt do not change within the experimental error.

III. CONCLUSIONS

In summary, spin transport in the as-grown disordered magnetic amorphous YIG film has been systematically investigated by the nonlocal spin-pumping ISHE experiments with horizontal and vertical geometries at room temperature. In the horizontal nonlocal devices with a gap from 2.0 μm to 200 nm, the nonlocal spin-pumping ISHE voltage signal is not detected within a 10 nV noise level. The small ST-FMR voltage signal is observed in the vertical geometry with a thin a-YIG spacer ($t \leqslant 30$ nm) and gradually reduces to near zero with the a-YIG thickness increasing to 40 nm. We interpret that the small voltage signal is caused by spin-rectification voltage in the bottom layer Py due to the electric leakage between the Pt and Py layers through the pinhole defects in the thin a-YIG middle layer. All nonlocal spin-pumping ISHE experiments confirm that the as-grown amorphous YIG does not possess long-distance spin transport. However, a considerable spin accumulation in the interface of a-YIG/Py is verified by the analysis of interfacial spin-mixing conductance and current-induced SOTs in the controlled experiments between a-YIG/Py/Pt and Py/Pt devices. The interface spin accumulation can be used as an efficient approach to improve SOT efficiency in the ferromagnet/heavy metal systems by adding disordered magnetic a-YIG as the buffer layer.

ACKNOWLEDGMENTS

[1] B. Heinrich, C. Burrowes, E. Montoya, B. Kardasz, E. Girt, Y. Y. Song, Y. Sun, and M. Wu, Phys. Rev. Lett. **107**, 066604 (2011).

[2] H. L. Wang, C. H. Du, Y. Pu, R. Adur, P. C. Hammel, and F. Y. Yang, Phys. Rev. B **88**, 100406(R) (2013).

[3] J. C. Gallagher, A. S. Yang, J. T. Brangham, B. D. Esser, S. P. White, M. R. Page, K. Y. Meng, S. S. Yu, R. Adur, W. Ruane, S. R. Dunsiger, D. W. McComb, F. Y. Yang, and P. C. Hammel, Appl. Phys. Lett. **109**, 072401 (2016).

[4] S. Azzawi, A. T. Hindmarch, and D. Atkinson, J. Phys. D Appl. Phys. **50**, 473001 (2017).

[5] F. Yang and P. C. Hammel, J. Phys. D Appl. Phys. **51**, 253001 (2018).

[6] Y. Kajiwara, K. Harii, S. Takahashi, J. Ohe, K. Uchida, M. Mizuguchi, H. Umezawa, H. Kawai, K. Ando, K. Takanashi, S. Maekawa, and E. Saitoh, Nature (London) **464**, 262 (2010).

[7] B. L. Giles, Z. Yang, J. S. Jamison, and R. C. Myers, Phys. Rev. B **92**, 224415 (2015).

[8] L. J. Cornelissen, J. Liu, R. A. Duine, J. B. Youssef, and B. J. van Wees, Nat. Phys. **11**, 1022 (2015).

[9] D. Wesenberg, T. Liu, D. Balzar, M. Wu, and B. L. Zink, Nat. Phys. **13**, 987 (2017).

[10] H. Ochoa, R. Zarzuela, and Y. Tserkovnyak, Phys. Rev. B **98**, 054424 (2018).

[11] J. M. Gomez-Perez, K. Oyanagi, R. Yahiro, R. Ramos, L. E. Hueso, E. Saitoh, and F. Casanova, Appl. Phys. Lett. **116**, 032401 (2020).

[12] R. Xiang, L. Chen, S. Zhang, H. Li, J. Du, Y. W. Du, and R. H. Liu, Mater. Res. Express **7**, 046105 (2020).

[13] L. Yang, Y. Fei, K. Zhou, L. Chen, Q. Fu, L. Li, C. Yan, H. Li, Y. Du, and R. Liu, Appl. Phys. Lett. **118**, 032405 (2021).

[14] Q.-H. Yang, H.-W. Zhang, Q.-Y. Wen, and Y.-L. Liu, J. Appl. Phys. **108**, 073901 (2010).

[15] S. Xia, S. Zhang, Z. Luan, L. Zhou, J. Liang, G. Liu, B. Yang, H. Yang, R. Liu, and D. Wu, Appl. Phys. Lett. **116**, 052404 (2020).

[16] C. Hauser, T. Richter, N. Homonnay, C. Eisenschmidt, M. Qaid, H. Deniz, D. Hesse, M. Sawicki, S. G. Ebbinghaus, and G. Schmidt, Sci. Rep. **6**, 20827 (2016).

[17] K. S. Das, W. Y. Schoemaker, B. J. van Wees, and I. J. Vera-Marun, Phys. Rev. B **96**, 220408(R) (2017).

[18] Y. Tserkovnyak, A. Brataas, and G. E. W. Bauer, Phys. Rev. B **66**, 224403 (2002).

[19] Y. Tserkovnyak, A. Brataas, and G. E. W. Bauer, Phys. Rev. Lett. **88**, 117601 (2002).

[20] Z. Feng, J. Hu, L. Sun, B. You, D. Wu, J. Du, W. Zhang, A. Hu, Y. Yang, D. M. Tang, B. S. Zhang, and H. F. Ding, Phys. Rev. B **85**, 214423 (2012).

[21] E. Saitoh, M. Ueda, H. Miyajima, and G. Tatara, Appl. Phys. Lett. **88**, 182509 (2006).

[22] L. Liu, T. Moriyama, D. C. Ralph, and R. A. Buhrman, Phys. Rev. Lett. **106**, 036601 (2011).

[23] J. Zhou, X. Wang, Y. Liu, J. Yu, H. Fu, L. Liu, S. Chen, J. Deng, W. Lin, X. Shu, H. Y. Yoon, T. Hong, M. Matsuda, P. Yang, St. Adams, B. Yan, X. Han, and J. Chen, Sci. Adv. **5**, eaau6696 (2019).

[24] Y. Wang, R. Ramaswamy, and H. Yang, J. Phys. D Appl. Phys. **51**, 273002 (2018).

[25] M. Harder, Y. Gui, and C.-M. Hu, Phys. Rep. **661**, 1 (2016).

[26] O. Mosendz, J. E. Pearson, F. Y. Fradin, G. E. W. Bauer, S. D. Bader, and A. Hoffmann, Phys. Rev. Lett. **104**, 046601 (2010).

[27] O. Mosendz, V. Vlaminck, J. E. Pearson, F. Y. Fradin, G. E. W. Bauer, S. D. Bader, and A. Hoffmann, Phys. Rev. B **82**, 214403 (2010).

[28] H. Nakayama, K. Ando, K. Harii, T. Yoshino, R. Takahashi, Y. Kajiwara, K. Uchida, Y. Fujikawa, and E. Saitoh, Phys. Rev. B **85**, 144408 (2012).

[29] S. Keller, J. Greser, M. R. Schweizer, A. Conca, V. Lauer, C. Dubs, B. Hillebrands, and E. T. Papaioannou, Phys. Rev. B **96**, 024437 (2017).

[30] H. Nakayama, M. Althammer, Y. T. Chen, K. Uchida, Y. Kajiwara, D. Kikuchi, T. Ohtani, S. Geprags, M. Opel, S. Takahashi, R. Gross, G. E. W. Bauer, S. T. B. Goennenwein, and E. Saitoh, Phys. Rev. Lett. **110**, 206601 (2013).

[31] T. O. Hongyu An, Y. Kanno, Y. Kageyama, Y. Monnai, H. Maki, Ji Shi, and K. Ando, Sci. Adv. **4**, eaar2250 (2018).

[32] H. An, Y. Kageyama, Y. Kanno, N. Enishi, and K. Ando, Nat. Commun. **7**, 13069 (2016).

[33] K. M. Law, S. Budhathoki, S. Ranjit, F. Martin, A. S. Thind, R. Mishra, and A. J. Hauser, Sci. Rep. **10**, 18357 (2020).

[34] W. Wang, T. Wang, V. P. Amin, Y. Wang, A. Radhakrishnan, A. Davidson, S. R. Allen, T. J. Silva, H. Ohldag, D. Balzar, B. L. Zink, P. M. Haney, J. Q. Xiao, D. G. Cahill, V. O. Lorenz, and X. Fan, Nat. Nanotechnol. **14**, 819 (2019).

[35] A. Davidson, V. P. Amin, W. S. Aljuaid, P. M. Haney, and X. Fan, Phys. Lett. A **384**, 126228 (2020).

[36] M. B. Jungfleisch, A. V. Chumak, A. Kehlberger, V. Lauer, D. H. Kim, M. C. Onbasli, C. A. Ross, M. Kläui, and B. Hillebrands, Phys. Rev. B **91**, 134407 (2015).

[37] J. C. Rojas-Sanchez, N. Reyren, P. Laczkowski, W. Savero, J. P. Attane, C. Deranlot, M. Jamet, J. M. George, L. Vila, and H. Jaffres, Phys. Rev. Lett. **112**, 106602 (2014).

[38] O. Mosendz, J. E. Pearson, F. Y. Fradin, S. D. Bader, and A. Hoffmann, Appl. Phys. Lett. **96**, 022502 (2010).

[39] M. F. Jakobsen, A. Qaiumzadeh, and A. Brataas, Phys. Rev. B **100**, 134431 (2019).

[40] J. C. Sanchez, L. Vila, G. Desfonds, S. Gambarelli, J. P. Attane, J. M. De Teresa, C. Magen, and A. Fert, Nat. Commun. **4**, 2944 (2013).

[41] A. Conca, S. Keller, M. R. Schweizer, E. T. Papaioannou, and B. Hillebrands, Phys. Rev. B **98**, 214439 (2018).

[42] K. Gupta, R. J. H. Wesselink, R. Liu, Z. Yuan, and P. J. Kelly, Phys. Rev. Lett. **124**, 087702 (2020).

[43] K. U. Demasius, T. Phung, W. Zhang, B. P. Hughes, S. H. Yang, A. Kellock, W. Han, A. Pushp, and S. S. P. Parkin, Nat. Commun. **7**, 10644 (2016).

[44] K. Ando, S. Takahashi, K. Harii, K. Sasage, J. Ieda, S. Maekawa, and E. Saitoh, Phys. Rev. Lett. **101**, 036601 (2008).

[45] C.-F. Pai, L. Liu, Y. Li, H. W. Tseng, D. C. Ralph, and R. A. Buhrman, Appl. Phys. Lett. **101**, 122404 (2012).

[46] D. Lee, W. Jeong, D. Yun, S. Y. Park, B. K. Ju, K. J. Lee, B. C. Min, H. C. Koo, and O. Lee, ACS Appl. Mater. Interfaces **13**, 19414 (2021).

[47] L. Frangou, G. Forestier, S. Auffret, S. Gambarelli, and V. Baltz, Phys. Rev. B **95**, 054416 (2017).